THE JOURNAL OF PHYSICAL CHEMISTRY C
A JOURNAL OF THE AMERICAN CHEMICAL SOCIETY

pubs.acs.org/JPCC

Article

Effect of Synthesis Temperature on Water Adsorption in UiO-66 Derivatives: Experiment, DFT+D Modeling, and Monte Carlo Simulations

Gabriela Jajko,* Patrycja Gryta, Paweł Kozyra,* Monika Szufla, Dariusz Matoga, Dorota Majda, and Wacław Makowski

Cite This: *J. Phys. Chem. C* 2022, 126, 9185−9194

Read Online

ACCESS | Metrics & More | Article Recommendations | Supporting Information

ABSTRACT: In this work, density functional theory (DFT) and Monte Carlo calculations were combined with standard volumetric adsorption as well as quasi-equilibrated temperature-programmed desorption and adsorption measurements to study water adsorption in UiO-66 derivatives containing $-NH_2$, $-NO_2$, and −Br substituents. Based on DFT modeling, both the position and geometry of the substituents were determined and one model was selected for each structure. By using Monte Carlo simulations and the force field developed in our previous work for the adsorption of water in metal−organic frameworks, we reproduced experimental adsorption isotherms and isobars. The results allow us to explain the water adsorption process in UiO-66 derivatives. Detailed physicochemical characterization by means of elemental analysis, powder X-ray diffraction, infrared spectroscopy, and thermogravimetric analysis enabled us to determine the influence of the synthesis temperature on the structure and properties of the materials.

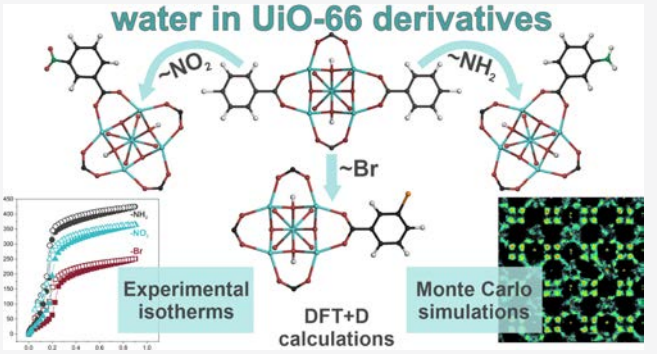

INTRODUCTION

Metal−organic frameworks (MOFs) are porous coordination polymers constructed with metal nodes interconnected by organic linkers.[1,2] Over the past two decades, MOFs have attracted a lot of attention due to their potential use in gas storage, separation, and catalysis.[3−5] An attractive aspect of the synthesis of MOF materials is the modification of organic linkers in order to introduce the desired functionality. However, optimization of synthesis conditions (e.g., temperature) to control crystallinity, morphology, and defects is still a challenge.

Following the discovery of UiO-66,[6] the zirconium(IV) oxide cluster family of MOFs gained much interest due to their high stability and functionality.[6−9] Unmodified UiO-66 consists of zirconium clusters connected by 1,4-benzenedicarboxylate (bdc^{2-}) ligands. In order to increase the application possibilities, syntheses of modified MOFs, e.g., UiO-66-NH_2,[10−12] UiO-67-$(NH_2)_2$,[13] UiO-66-Br,[14] or UiO-66-NO_2,[15] have been developed. Although many materials are unstable in contact with water vapor, the UiO-66 family has been proven to be highly hydrothermally stable,[16−19] making it an ideal candidate as a water adsorbent.

The water adsorption properties of porous materials have been a topic actively explored for several years. In particular, these properties are considered in the context of heat pumps, e.g., for use in vehicular air-conditioning units[20−23] or in water harvesting.[17,24,25] In all these water capture applications, several criteria must be considered when selecting a porous material. First, the filling of the pores must occur as a steep uptake at low p/p_0. This is important primarily because the water in the air is present in low concentrations. Second, the sorption capacity of the material must be high, and third, the material must be highly stable at high temperatures and in contact with water.[26] Finding an ideal material for water adsorption that meets all these criteria is time-consuming. For example, microporous zeolites used so far for this purpose require a prohibitively high temperature of regeneration due to their strong interaction with water molecules. Mesoporous materials, on the other hand, adsorb water only at high pressures.[27] Computationally, water adsorption is also challenging due to strong and specific interaction both between guest molecules and between water and adsorbents. Independently on the level of modeling, implementing proper interaction for water remains tough. Either for classical

Received: April 5, 2022
Revised: April 27, 2022
Published: May 18, 2022

https://doi.org/10.1021/acs.jpcc.2c02315
J. Phys. Chem. C 2022, 126, 9185−9194

modeling or quantum calculations, applied potential, parametrization, model, and precision are the key features. Sometimes still this is not enough, and researchers for describing H-bond effects have to include also dynamic and coupling effects, which must be considered beyond the Born-Oppenheimer approximation. More sophisticated approaches combine both classical and quantum simulations; *e.g.*, recent work by Paesani's group has taken a different approach, including D_2O.[28] Using infrared spectroscopy (IR) spectroscopy and simulations of both classical molecular dynamics (MD) and centroid molecular dynamics (CMD), it has been proved that literature force fields, commonly used in simulations, are not able to correctly represent the strength of the framework−water interactions.

The aim of this work was to study the adsorption of water in $-NH_2$, $-NO_2$, and −Br-substituted UiO-66, synthesized at different temperatures. Previous studies showed that the synthesis temperature for unmodified UiO-66 strongly influences its crystallinity and the number of structural defects.[29] For the experimental investigation of water adsorption, both classical volumetric experiments and measurements by means of the innovative quasi-equilibrated temperature-programmed desorption and adsorption (QE-TPDA)[30−32] were employed. In addition, density functional theory (DFT) modeling and molecular Monte Carlo simulations were performed to better understand the mechanism of water adsorption in UiO-66 derivatives.

METHODS

All chemicals and solvents were purchased from commercial sources (Merck, Fluorochem) and were used without further purification. Syntheses of UiO-66-X-*T* materials (X denotes a substituent, and *T* denotes the synthetic temperature) with varying contents of defects were carried out according to the following procedures:[6,33] 0.55 mmol $ZrCl_4$ (128 mg) and 0.55 mmol H_2BDC-X were dissolved in 15 mL of *N*,*N*′-dimethylformamide (DMF); 2.26 mmol 35% HCl (0.20 mL) was added, and the solutions were transferred to 20 mL Teflon liners and heated in stainless-steel autoclaves at 120, 170, or 220 °C for 24 h. The resulting powders of UiO-66-X-*T* were filtered off and washed using 20 mL of DMF with stirring at 100 °C for 60 min. After washing, the samples were filtered off and dried for 1−2 h at 80 °C. Then, 15−20 mg of each product was subjected to thermogravimetric analysis (TGA) characterization, and the rest was used for other measurements including adsorption measurements. Table 1 summarizes the codes of samples, quantities of H_2BDC-X acids, and the temperature during synthesis. Based on the previous research,[29] by performing synthesis at different temperatures we attempted to obtain UiO-66 derivatives containing the lowest content of structural defects.

Table 1. Sample Codes, Amounts of H_2BDC-X Acids Used, and Synthesis Temperatures

sample name	H_2BDC-X/mg		reaction temperature/°C
UiO-66-NH_2-120	H_2BDC-NH_2	99.6	120
UiO-66-NH_2-170			170
UiO-66-NH_2-220			220
UiO-66-NO_2-120	H_2BDC-NO_2	116	120
UiO-66-NO_2-170			170
UiO-66-NO_2-220			220
UiO-66-Br-120	H_2BDC-Br	135	120
UiO-66-Br-170			170
UiO-66-Br-220			220

The CHN elemental analyses (EA) were performed with standard microanalysis procedures using an Elementar Vario Micro Cube CHN analyzer (Table S2 in the Supporting Information).

Fourier-transform infrared spectroscopy (FT-IR) spectra were recorded on a Thermo Scientific Nicolet iS10 FT-IR spectrophotometer equipped with an iD7 diamond ATR attachment in a wavenumber range from 4000 to 500 cm^{-1} with 32 scans.

Powder X-ray diffraction (PXRD) patterns were recorded at room temperature (295 K) using a Rigaku Miniflex 600 diffractometer with Cu-K α radiation (λ = 1.5418 Å) in a 2θ range from 5 to 45° with a 0.02° step and 3 °/min scan speed.

Before thermogravimetric and sorption measurements, DMF remaining in the as-synthesized UiO-66-X-*T* samples was removed by methanol exchange. Each sample was immersed in 10 mL of methanol and kept at 60 °C for 2−3 days. During this period, methanol was changed at least two times.

TGA was performed using a Mettler-Toledo TGA/SDTA 851e instrument with a heating rate of 10 °C/min in a temperature range of 25−1000 °C (approx. sample weight of 10 mg). The measurements were performed at atmospheric pressure, under air flow (Table S1 in the Supporting Information).

Adsorption isotherms were measured using a static volumetric Autosorb IQ apparatus (Quantachrome Instruments) at 77 K for nitrogen and 293 K for water. Prior to the measurements, all samples were activated under vacuum for 8 h at 100 °C (2 °C/min). Specific surface areas were determined from isotherms using the BET method. Pore volumes were obtained using the t-plot method.

Adsorption of water was additionally studied in subsequent cycles of adsorption and desorption using the quasi-equilibrated temperature programmed desorption and adsorption (QE-TPDA) technique.[30,31] Samples of ca. 5 mg of the MOFs were activated by heating in a flow (6.5 cm^3/min) of pure helium (purity 5.0, Air Products) at 200 °C (ramp 10 °C/min). After the activation, the gas flow was switched to a mixture of helium and water vapor saturated at room temperature, which results in isothermal adsorption at room temperature. After stabilization of the thermal conductivity detector signal, the QE-TPDA experiment was performed by heating and cooling the sample in the flow of the He/H_2O mixture according to the linear temperature program with 1 and 2 °C/min temperature change rates. Sorption capacities were determined by integrating desorption maxima over the range from 25 to 120 °C and recalculating the obtained areas by an adequate calibration constant.[32] Desorption and adsorption integral profiles (which may be regarded as approximate isobars) were calculated from the integrated QE-TPDA desorption and adsorption profiles recorded at 1 °C/min. A more detailed description of the QE-TPDA apparatus and experimental procedures were reported elsewhere.[30−32]

Quantum-chemical calculations of energies and geometries for UiO-66 derivatives were performed with the use of DMol3 code[34] at the periodic DFT level of theory. We used the RPBE[35,36] correlation−exchange functional, and the orbitals were expanded in the DND basis set with DSPP pseudopotentials.[37] We set the basis spatial cut-off distance

https://doi.org/10.1021/acs.jpcc.2c02315
J. Phys. Chem. C 2022, 126, 9185−9194

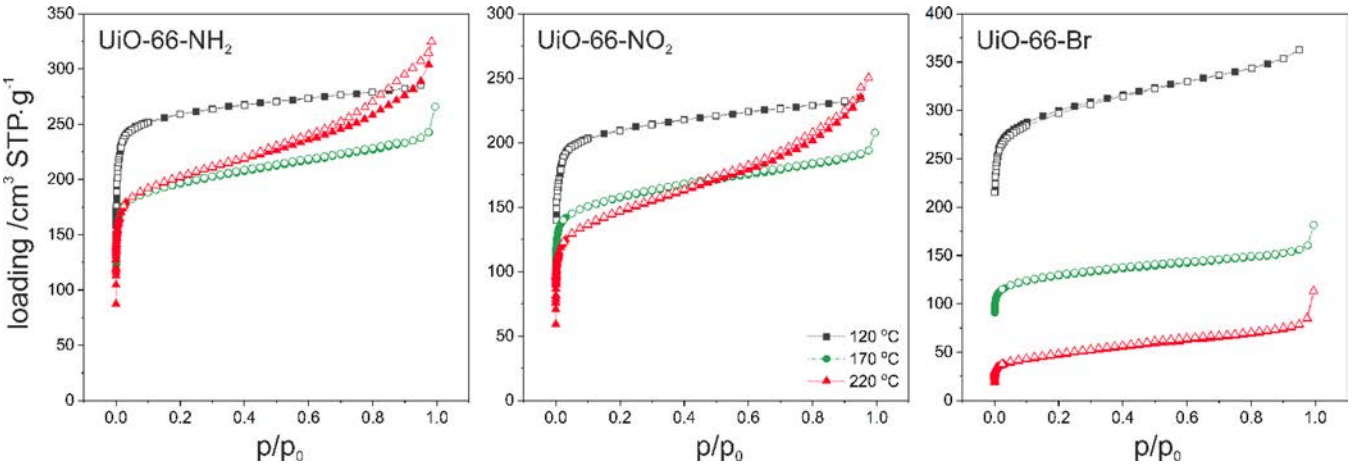

Figure 1. Experimental adsorption isotherms of nitrogen in UiO-66-X derivatives measured at 77 K.

as 4.2 Å and Gaussian smearing with a width of 5×10^{-3} Ha. The SCF convergence criterion was set to 1×10^{-5} Ha, maximal force was lower than 4×10^{-3} Ha/Å, and the maximal atom displacement was lower than 5×10^{-3} Å. The Γ-point-only sampling of the irreducible part of the first Brillouin zone was used.

Adsorption isotherms were calculated using Monte Carlo simulations in the grand-canonical ensemble (GCMC). The pressure is related to the volatility according to the Peng-Robinson equation of state.[38] All simulations were performed in the $2 \times 2 \times 2$ unit cells with 1×10^5 initialization cycles and 1×10^6 production cycles with equal probabilities of translation, rotation, swap, and reinsertion. We used a Widom particle-insertion method[39] at zero coverage to calculate heats of adsorption, pore volumes, and helium void fractions. Simulations were performed using the RASPA code.[40,41]

In this work, we used the TiP4P-Ew[42] model for the water molecule (Table S3 in the Supporting Information). The structures were modeled as rigid crystals. Lennard-Jones parameters for the framework were taken from the DREIDING[43] force field for carbon, oxygen, hydrogen, nitrogen, and bromine and from UFF[44] for zirconium. Point charges for the framework were taken from previously developed force field,[29] by applying the same procedure. The atom types of our models and a full set of charges are available in Figure S1 and Table S4 in the Supporting information, respectively. Guest−host interactions were calculated with the standard Lorentz-Berthelot mixing rules. The Lennard-Jones cut-off distance was set at 12 Å. Coulombic interactions were computed by using the Ewald summation method with a relative precision of 10^{-6}.

RESULTS AND DISCUSSION

Physicochemical Analysis. The syntheses of three UiO-66 derivatives were performed at 120, 170, and 220 °C. For clarity, the samples were labeled as UiO-66-X-120, UiO-66-X-170, and UiO-66-X-220, respectively (where X = NH_2, NO_2, Br). The elemental analysis of the samples may be found in Table S2. The parent UiO-66, without substituents, was labeled as UiO-66-*T* (*T* = 100, 160, 220 °C), as in the previous work.[29] The results of structural analysis by means of PXRD (Figure S2 in the Supporting Information) show that the UiO-66 structure is preserved for all materials. The patterns corresponding to 120 and 170 °C are very similar for all the samples; however, in the case of 220 °C, a gentle bump (the highest for UiO-66-Br) on the background can be observed, which may indicate the presence of the amorphous phase or residue of the 1,4-bdc linker. Less-intensive background bumps, due to the presence of an amorphous phase, are also noticeable for the other -Br samples. The PXRD results obtained for the materials synthesized at 220 °C are in contrast with the previously reported findings showing that the synthesis of the unmodified material at 220 °C leads to the formation of the pure UiO-66 phase without missing linker defects.[29,45]

Table 2. Characteristics of UiO-66 Derivatives, Including BET Surface Areas, Micropore Volumes (PV), and External Surface Areas (S_{ext})

	BET/$m^2 \cdot g^{-1}$	PV/$cm^3 \cdot g^{-1}$	S_{ext}/$m^2 \cdot g^{-1}$
UiO-66-NH_2-120	1042	0.309	45
UiO-66-NH_2-170	767	0.228	52
UiO-66-NH_2-220	769	0.211	104
UiO-66-NO_2-120	836	0.239	48
UiO-66-NO_2-170	606	0.177	41
UiO-66-NO_2-220	542	0.129	129
UiO-66-Br-120	1161	0.317	116
UiO-66-Br-170	496	0.147	39
UiO-66-Br-220	167	0.026	35

The varying number of -OH groups in each sample, manifested by the intensity of an IR band at ca. 3400 cm^{-1}, may correlate with the number of missing linker defects (Figure S3 in the Supporting Information). The more intense the band is, the more missing linker defects are present, assuming the same amount of hydroxylic solvent molecules in the samples. For UiO-66-NH_2, the least intense band is observed for the material synthesized at 170 and 220 °C, which can indicate the smallest number of structural defects. On the other hand, this band is the strongest for UiO-66-NH_2-120. The same trend is observed for the UiO-66-NO_2 samples. Only for UiO-66-Br materials, there is a clear difference between sample −170 and −220. However, the most optimal synthesis temperature appears to be 170 °C for all samples, since such materials are characterized by the band at 3400 cm^{-1} of the lowest intensity.

During the TGA analysis (Figure S4 in the Supporting Information), three stages of mass loss can be observed. The

https://doi.org/10.1021/acs.jpcc.2c02315
J. Phys. Chem. C 2022, 126, 9185−9194

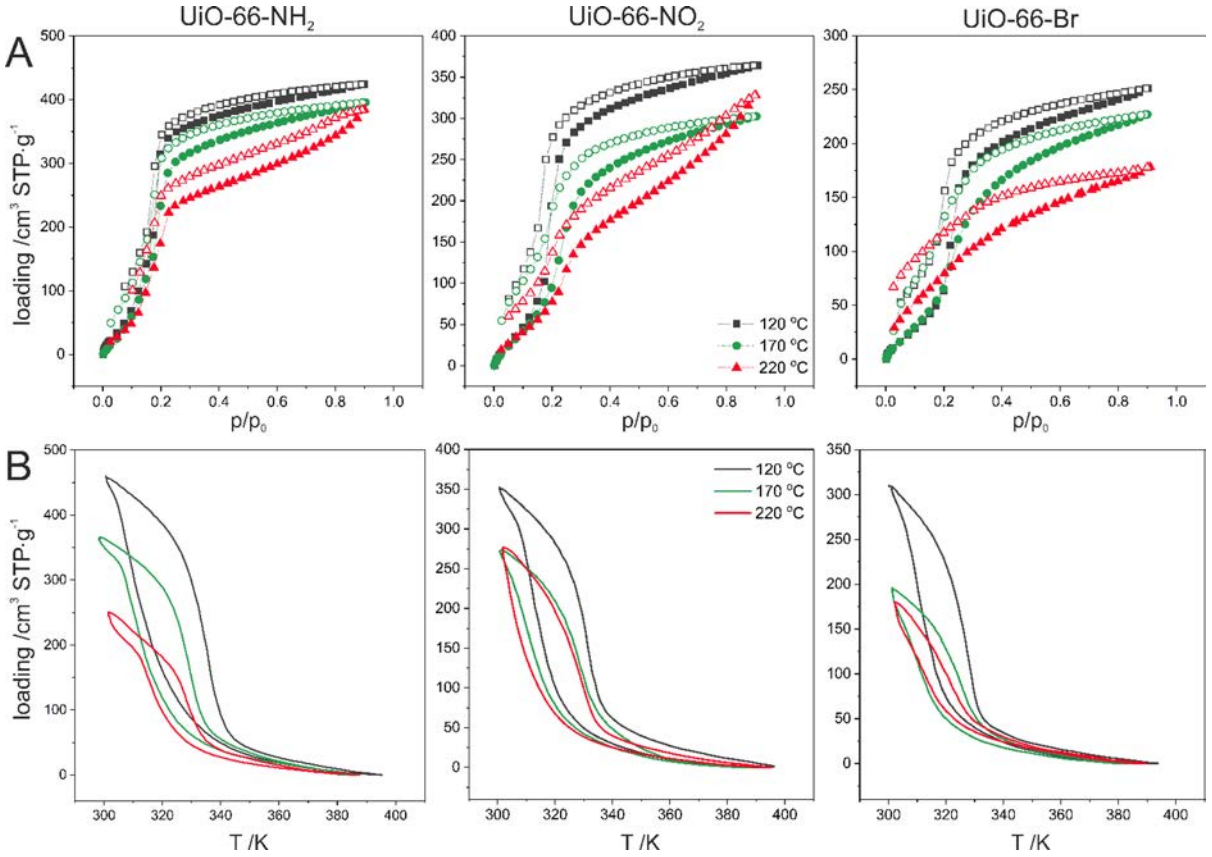

Figure 2. (A) Experimental adsorption−desorption isotherms and (B) QE-TPDA-based integral adsorption and desorption profiles of water in UiO-66-X derivatives measured at 293 K and 2.4 kPa, respectively.

first one occurs in the temperature range from 25 to 100 °C, where the solvent residues are desorbed. Next, a plateau-like mass loss step, in the 100−300 °C range (100−400 °C in the case of UiO-66-Br-120 and -170), results from gradual removal of linkers. The final mass loss, corresponding to a decomposition of the frameworks and oxidation or desorption of the linkers, is observed in the range of about 400−550 °C.[46] Based on an experimental residue mass, which in each case contains ZrO_2 only, we calculated the expected stoichiometric amounts of the ideal MOFs with empty pores (dashed lines, Figure S4 in the Supporting Information). The comparisons of these amounts with the observed experimental values clearly show that all samples synthesized at 220 °C contain less than 50% of the expected amount of organic linkers. Therefore, the amorphous contaminations, the presence of which is evidenced by PXRD, are enriched in zirconium, as compared to the ideal material. The IR spectra (Figure S3 in the Supporting Information) for the samples synthesized at 220 °C contain an additional distinct band at 1282 cm^{-1}, attributed to symmetric stretching of monodentate-bound carboxylates. The amount of this form of carboxylates increases with the temperature of synthesis as well as in the order NH_2 < NO_2 < Br. Moreover, based on the results of elemental analysis and TGA measurements, the chemical formulas for all samples were determined (Table S1 and S2 in the Supporting Information). It was shown that for UiO-66-NH_2 and UiO-66-NO_2 samples for the synthesis temperatures of 120 and 170 °C, the percent of the defects reached a maximum of 6%, and for a temperature of 220 °C, it was over 30%. In the case of UiO-66-Br samples, about 10% of defects appear already at the lowest temperature, and at a temperature of 220 °C, the percentage of defects reaches 45%.

In order to characterize the porosity of the UiO-66-X materials, we measured nitrogen adsorption isotherms (Figure 1). On their basis, the values of the BET specific surface areas and pore volumes were determined and are presented in Table 2. The largest BET surface area was calculated for the UiO-66-X-120 samples. In contrast, the lowest specific surface area was observed for the UiO-66-X-220 samples, with the only exception for UiO-66-NH_2, where the surface areas were similar for the samples synthesized at 170 and 220 °C. These values together with the lowest micropore volumes as well as the presence of amorphous phases detected by PXRD indicate that a synthesis temperature of 220 °C is too high and results in the formation of imperfect, partially collapsed UiO-66-X structures.

Previous literature studies showed that for the unsubstituted UiO-66, the highest sorption capacity was associated with the highest number of defects (for UiO-66-100); while at 220 °C, the material with the lowest degree of defects was obtained (UiO-66-220).[29] In the case of UiO-66 derivatives, a similar relationship can be found; however, for different temperatures, similarly, the lowest synthesis temperature (120 °C) corresponds to high sorption capacity, while the least "defective" structure is obtained at 170 °C. A higher synthesis temperature does not lead to the material with the lowest number of defects (as was the case for UiO-66-220); on the contrary, the material is already somewhat amorphous, and its microporosity is reduced.

https://doi.org/10.1021/acs.jpcc.2c02315
J. Phys. Chem. C 2022, 126, 9185−9194

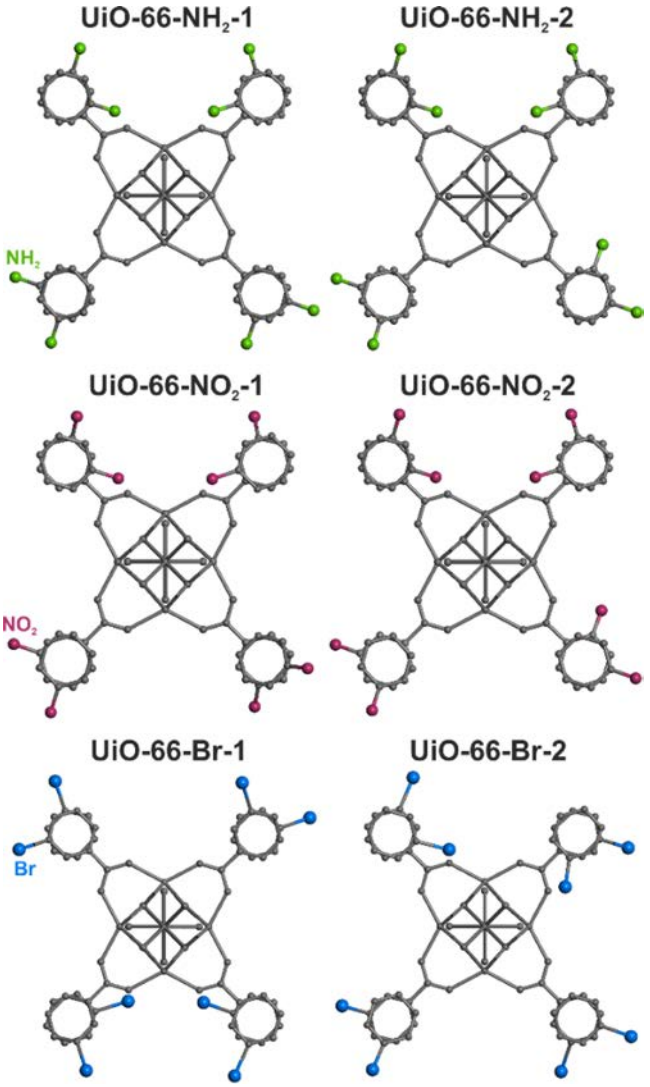

Figure 3. Schematic representation of the distribution of ring substituents in the UiO-66-X structures.

Table 3. Relative Energy of UiO-66-X Models, where X = NH_2, NO_2, Br after Optimization by the DFT+D Method

model	relative energy/kcal·mol^{-1}
UiO-66-NH_2−1	**0**
UiO-66-NH_2−2	+403.8
UiO-66-NO_2−1	**0**
UiO-66-NO_2−2	+451.9
UiO-66-Br-1	+0.2
UiO-66-Br-2	**0**

Table 4. GCMC-Based Characteristics of the Structures Used in This Work, Where PV is the Pore Volume and HVF is the Helium Void Fraction[a]

	UiO-66-NH_2	UiO-66-NO_2	UiO-66-Br
HVF	0.4820	0.4096	0.4673
PV/cm^3·g^{-1}	0.3670	0.2829	0.2920
cell lengths/Å ($a = b = c$)	20.7	20.7	20.7
cell angles/° ($\alpha = \beta = \gamma$)	90	90	90
framework density/kg·m^{-3}	1313	1447	1600

[a]All parameters are given for 2 × 2 × 2 supercells.

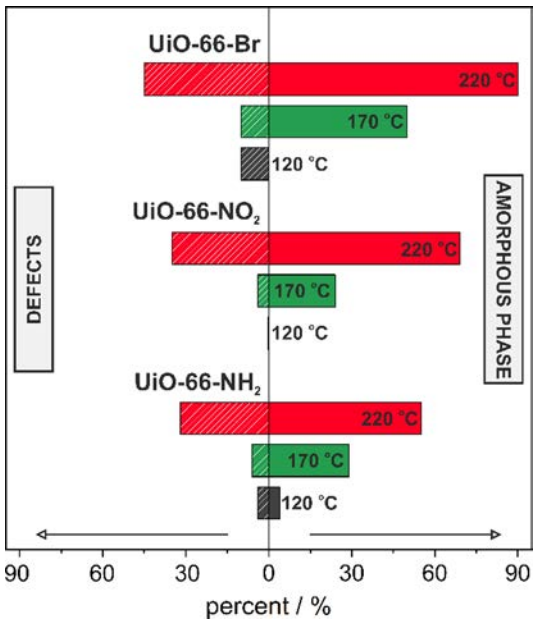

Figure 4. Percent amounts of missing-linker defects and the amorphous phase in UiO-66-X samples.

Water Adsorption. Experimental adsorption isotherms of water in the UiO-66-X materials are presented in Figure 2A. The observed effect of the synthesis temperature on nitrogen sorption is even more visible in the case of water adsorption. For the materials obtained at 120 and 170 °C, the isotherms follow a typical type V shape. The lower the synthesis temperature, the higher the water adsorption capacity, and therefore, the hydrophilicity is increased. Comparing the least-defective materials (UiO-66-220 and UiO-66-X-120), it is possible to assess the effect of the ring substituent on water adsorption in the decreasing order of adsorption capacities: −H > −NH_2 > −NO_2 > −Br. What is more, it can be observed that the samples synthesized at 220 °C have the lowest sorption capacities, and in particular, UiO-66-Br-220 has the lowest BET surface area and micropore volume of all samples.

For the −NH_2 structures, steep water uptake occurs at a relative partial pressure p/p_0 between 0.1 and 0.2, and for the −NO_2 and −Br ones, except for the "-220" samples, it occurs at p/p_0 from 0.15 to 0.3. Another effect is that the capacities of the UiO-66-X-120 series are much higher as compared to the rest. In summary, the UiO-66-X-220 samples show the lowest sorption capacity due to the presence of amorphous zirconium phases. UiO-66-NH_2-120 has the highest water sorption capacity of all the samples.

The isothermal water adsorption experiments were supplemented with QE-TPDA measurements (Figures S5−S7). The QE-TPDA profiles consist of desorption maxima and adsorption minima, corresponding to the temporary amount of water vapor desorbed or adsorbed at a given pressure. The hysteresis between desorption and adsorption may be an inherent feature of the adsorbent−adsorbate system, resulting from the different mechanisms of these two processes. A similar behavior (i.e., adsorption−desorption hysteresis) is observed in the isothermal measurements by the standard volumetric method (Figure 2A). Integral desorption and adsorption curves (Figure 2B) calculated from QE-TPDA profiles reproduce general trends observed in static isothermal measurements for all samples, with those synthesized at 120 °C

https://doi.org/10.1021/acs.jpcc.2c02315
J. Phys. Chem. C 2022, 126, 9185−9194

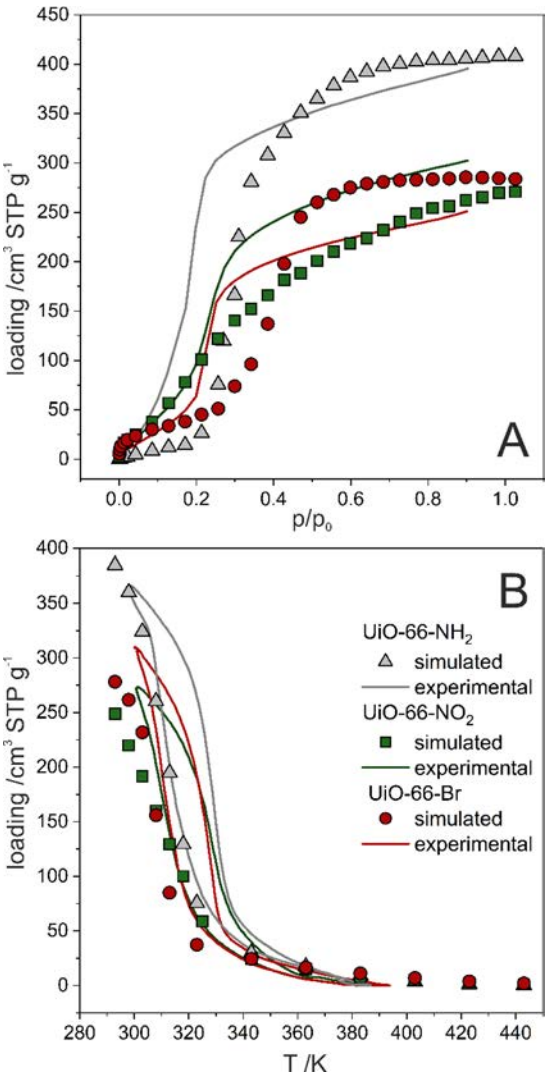

Figure 5. Comparison of the simulated (points) and experimental (lines) adsorption (A) isotherms and (B) isobars of water in UiO-66-NH_2-170, UiO-66-NO_2-170, and UiO-66-Br-120 samples, at 293 K and 2.4 kPa, respectively.

showing the highest sorption capacity. Quantitative differences of the maximum sorption capacities found in the isothermal and thermodesorption measurements should be attributed to lower accuracy of the QE-TPDA data, resulting from relatively larger uncertainty of the smaller sample masses (ca. 5 mg).

DFT+D Calculations. Taking into account the fact that the exact position of the substituents in the aromatic rings of the linkers is unknown, and even more, their mutual arrangement in the unit cell, it was necessary to create models of structures with a different arrangement of substituents and to compare the energy of these structures. Thus, for each of the structures, two models were designed with a different arrangement of the $-NH_2$, $-NO_2$, and $-Br$ groups. The structures were then optimized, and the relative energies were calculated. For each structure, the model with the lowest energy was selected and used for further calculations. Due to the low steric hindrance, the energy difference between the structures for UiO-66-Br is not crucial, so these models are equivalent. The location of substituents in the initial and selected structures is shown in Figure 3. In Table 3, the relative energy after optimization is collected, the selected structures are marked in bold.

Monte Carlo Simulations. As shown in the literature, universal force fields cannot reproduce experimental results for water adsorption in MOFs.[29,47] For this reason, it was necessary to use the modified force field developed in the previous work.[29] The same procedure was used; i.e., the metal cluster charges were increased by 40%, leaving all the rest obtained by the EQeq method.[48] The full set of point charges is summarized in Table S4 in the Supporting Information. Characteristics of the tested systems are provided in Table 4.

A comparison of the simulated and experimental adsorption isotherms is shown in Figure S8A in the Supporting Information. In Figure S8B (Supporting Information) the calculated isobars are compared with the corresponding QE-TPDA-based integral adsorption and desorption curves (Figures S5−S7, Supporting Information). Based on the calculations with the increasing pressure, the heat of water adsorption was calculated (Figure S9 in the Supporting Information). As the structures used for calculations are defect-free, one can expect that the simulated isotherms should correspond to the experimental data for the materials synthesized at optimal temperatures. Indeed, for UiO-66-NH_2 and UiO-66-NO_2, the calculated pore volumes and sorption capacities are the closest to the experimental values for the samples synthesized at 120 °C.

Experimental samples are both to some extent defected and to some extent amorphous. Using the following methods, TGA, EA, volumetric gas adsorption, and MC modeling, we estimated both the number of missing-linker defects and the amount of amorphous phase in the studied samples. Based on TGA (Table S1), the missing-linker defect degree (d) was determined. These results together with elemental analyses allowed us to propose chemical formulas for the defective samples (Table S2).[45,49] The defective samples show an increased porosity, and it was assumed that the pore size grows proportionally with the defect degree. Based on the calculations for the defect-free and measurement for defective (with a significant and known defect degree d = 0.2) unsubstituted UiO-66,[29] the proportionality coefficient (β) between the defect degree (d) and the increase in the pore volume (ΔV_d) was determined:

$$\Delta V_d = \beta \cdot d \tag{1}$$

For the ideal UiO-66-220, this equation gives the number of defects (d = 1%), which is close to the expected zero value. In the case of partially amorphous (a) material, the increase in porosity results only from the defective crystalline contribution:

$$\Delta V_d = \beta \cdot d \cdot (1 - a) \tag{2}$$

The presence of the amorphous phase results in a reduction of the pore volume:

$$\Delta V_a = -a \cdot V_{\text{ideal}} \tag{3}$$

Due to the excellent agreement between the determined and calculated pore volume, the change in pore volume (ΔV) was calculated from the difference between the calculated pore volume for the ideal material and the experimentally measured volumes. Finally, from the relationship

$$\Delta V = \Delta V_d + \Delta V_a = \beta \cdot d \cdot (1 - a) - a \cdot V_{\text{ideal}} \tag{4}$$

it was possible to estimate the amount of the amorphous phase. The determined values are shown in Figure 4.

https://doi.org/10.1021/acs.jpcc.2c02315
J. Phys. Chem. C 2022, 126, 9185−9194

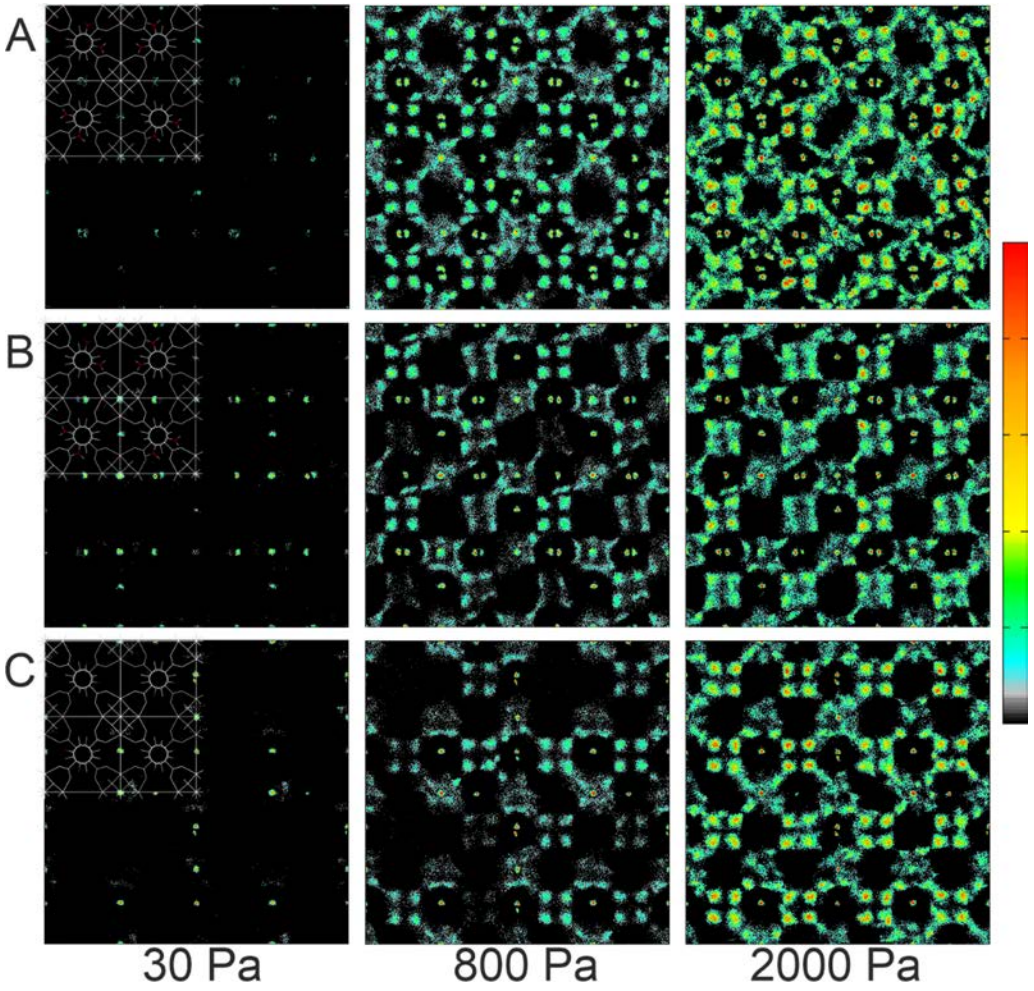

Figure 6. Average occupation profiles of water in (A) UiO-66-NH_2, (B) UiO-66-NO_2, and (C) UiO-66-Br structures at 293.15 K. For clarity, the UiO-66-X structure model has been superimposed.

While for the material UiO-66 without substituents, an increase in the synthesis temperature caused a decrease in the number of defects (synthesis at 220 °C led to a defect-free material); in the case of linkers with substituents, an increase in temperature causes an increase in the concentration of defects. Additionally, with temperature, the proportion of the amorphous phase increases significantly. The presence of considerable amounts of amorphous phases in the UiO-66-Br-220 and UiO-66-NO_2-220 samples, quantified using eq 4, is also clearly conspicuous in their PXRD patterns (Figure S2). Therefore, in contrast to the unsubstituted UiO-66, the optimal synthesis temperatures for the substituted analogues are *ca.* 120 °C. Consequently, the applied synthesis procedures do not allow us to increase the defect degree while maintaining the crystallinity.

Simultaneous quantification of defects and amorphousness allowed us to evaluate the effect of temperature on the quality of the samples obtained (Figure 4).

In the case of UiO-66-NO_2, steep part of the adsorption isotherm for synthesis at 170 °C is only slightly shifted to lower pressure, which indicates a low concentration of defects. Lower temperature (120 °C) shifts the isotherm to lower pressure. This phenomenon was also observed and studied for the parental UiO-66 as the effect of linker defects—the more defects the higher hydrophilicity and the lower pressure of the steep part of the isotherm.[29] This effect was also tested for the NH_2 derivative, for which the simulated isotherm did not agree with the low-pressure range of the experimental isotherm. For this purpose, 32 structural defects (*ca.* 20% of defects) in the 2 × 2 × 2 unit cell were introduced in the form of missing all linkers in every second layer in the *xy* direction and the water adsorption was calculated in the range from 0 to 0.25 p/p_0 (Figure S10 in the Supporting Information). As one can observe, after carrying out this modification, the low-pressure range goes in line with the experimental adsorption curve, which proves that all samples of the NH_2 derivative contain structural defects. This finding is consistent with the fact that the experimental adsorption heat for UiO-66-NH_2-170 in the low loading range is considerably larger than that found in the molecular simulations for the perfect structure, and for the structure with 32 defects, heat of adsorption achieves higher values. Thus, in general, the quality of substituted UiO-66 materials depends on a delicate balance between the presence of amorphous zirconium/organic phases and the presence of ligand defects (Figure 4). The amount of amorphous phases in the materials synthesized at 220 °C increases in the order UiO-66 < UiO-66-NH_2 < UiO-66-NO_2 < UiO-66-Br. On the other hand, the synthesis below the optimal temperature increases the concentration of defects. This information is in agreement with the content of the amorphous phases identified by IR spectroscopy.

https://doi.org/10.1021/acs.jpcc.2c02315
J. Phys. Chem. C 2022, 126, 9185−9194

The simulated adsorption isotherms (Figure 5) show the highest maximal uptake for UiO-66-NH_2, whereas for both UiO-66-NO_2 and UiO-66-Br, this uptake is lower and similar; however, the shape of isotherms at low pressures is different.

Figure 6 shows average occupation profiles for the UiO-66-X structures determined from calculations at 30, 800, and 2000 Pa, which represent distribution maps of water molecules per unit cell in the *xy* plane. It can be observed that guest molecules at low pressures fill the spaces around zirconium clusters, while at higher pressures, they accumulate around NH_2, NO_2, and Br substituents. A similar behavior was observed for the ideal structure of UiO-66.[29] The maps are somewhat "blurred" in the places where the substituents are located (for UiO-66-NH_2, this behavior is observed only at high pressures). This fact indicates that the interactions between water molecules and $-NH_2$, $-NO_2$, and −Br groups are much stronger than those with −CH groups of the aromatic rings.

Radial distribution functions (Figures S11−S13 in the Supporting Information) indicate that water molecules, despite the presence of ring substituents in organic linkers, prefer adsorption in the proximity of metal clusters.

For all structures, the distance from the center of mass of the water molecule from the zirconium atom was about 2.8 Å. Additionally, increasing the pressure does not affect the distance between water and ring substituents, which is 3 and 3.2 Å for UiO-66-Br and UiO-66-NO_2, respectively. The only exception is UiO-66-NH_2, for which at 30 Pa, the distance to the $-NH_2$ group is about 5 Å, and at 2000 Pa, it is reduced to about 3 Å. This different behavior for the amino-substituent goes in line with the simulated and experimental isotherm at the low-pressure region since water adsorption takes place on zirconium clusters solely (if it does) in this pressure range (Figure S10 in the Supporting Information). As charges on the zirconium clusters are independent of the model, the possible reason preventing adsorption at low pressure in UiO-66-NH_2 is a geometrical factor induced by the location of the substituents.

CONCLUSIONS

In this work, we have studied water adsorption in the series of UiO-66 derivatives, synthesized at different temperatures. The samples were characterized in terms of structure and porosity. Designing several structures with a different arrangement of ring substituents and optimizing them using the DFT+D (DMol3) formalism allowed for the selection of the most energetically advantageous structure. Moreover, using a previously developed set of framework charges,[29] adapted to the new structures, we calculated adsorption isotherms and isobars using the Monte Carlo method, which reproduced experimental data. The obtained results enabled us to explain the effect of the substituent and the presence of defects or the amorphous phase on adsorption isotherms and to indicate preferential adsorption sites. We have demonstrated that experiments supported by simulations give a deeper insight into materials' adsorption properties. Furthermore, our results support the idea that the UiO-66 family with functionalized linkers may be potential candidates for use in water harvesting applications.

ASSOCIATED CONTENT

Supporting Information

The Supporting Information is available free of charge at https://pubs.acs.org/doi/10.1021/acs.jpcc.2c02315.

Number of missing linkers calculated on the basis of thermogravimetric analysis; elemental analysis of UiO-66-X-*T* samples; proposed chemical formulas including estimated percentages of defects; guest−host interactions for a water molecule; list of charges of atoms in the frameworks; PXRD patterns; FTIR absorption spectra; TGA curves; sample masses and inlet pressures used in the QE-TPDA measurements; QE-TPDA profiles; experimental data (lines) and calculated (points) adsorption isotherms and isobars; and radial distribution functions (PDF)

AUTHOR INFORMATION

Corresponding Authors

Gabriela Jajko − *Faculty of Chemistry, Jagiellonian University in Kraków, Kraków 30-387, Poland;* orcid.org/0000-0001-8286-917X; Email: gabriela.jajko@doctoral.uj.edu.pl

Paweł Kozyra − *Faculty of Chemistry, Jagiellonian University in Kraków, Kraków 30-387, Poland;* orcid.org/0000-0002-7168-5022; Email: kozyra@chemia.uj.edu.pl

Authors

Patrycja Gryta − *Faculty of Chemistry, Jagiellonian University in Kraków, Kraków 30-387, Poland;* orcid.org/0000-0002-0198-6364

Monika Szufla − *Faculty of Chemistry, Jagiellonian University in Kraków, Kraków 30-387, Poland;* orcid.org/0000-0001-9099-3832

Dariusz Matoga − *Faculty of Chemistry, Jagiellonian University in Kraków, Kraków 30-387, Poland;* orcid.org/0000-0002-0064-5541

Dorota Majda − *Faculty of Chemistry, Jagiellonian University in Kraków, Kraków 30-387, Poland*

Wacław Makowski − *Faculty of Chemistry, Jagiellonian University in Kraków, Kraków 30-387, Poland;* orcid.org/0000-0002-4055-9664

Complete contact information is available at: https://pubs.acs.org/10.1021/acs.jpcc.2c02315

Author Contributions

The manuscript was written through contributions of all authors. All authors have given approval to the final version of the manuscript.

Notes

The authors declare no competing financial interest.

ACKNOWLEDGMENTS

The present study was funded by the National Science Centre Poland (grant 2018/29/B/ST4/00328).

REFERENCES

(1) Eddaoudi, M.; Kim, J.; Rosi, N.; Vodak, D.; Wachter, J.; O'Keeffe, M.; Yaghi, O. M. Systematic Design of Pore Size and Functionality in Isoreticular MOFs and Their Application in Methane Storage. *Science* **2002**, *295*, 469−472.

(2) Furukawa, H.; Cordova, K. E.; O'Keeffe, M.; Yaghi, O. M. The Chemistry and Applications of Metal-Organic Frameworks. *Science* **2013**, *341*, No. 1230444.

(3) Suh, M. P.; Park, H. J.; Prasad, T. K.; Lim, D. W. Hydrogen Storage in Metal-Organic Frameworks. *Chem. Soc. Rev.* **2012**, *112*, 782−835.
(4) Li, J. R.; Kuppler, R. J.; Zhou, H. C. Selective Gas Adsorption and Separation in Metal-Organic Frameworks. *Chem. Soc. Rev.* **2009**, *38*, 1477−1504.
(5) Farha, O. K.; Shultz, A. M.; Sarjeant, A. A.; Nguyen, S. T.; Hupp, J. T. Active-Site-Accessible, Porphyrinic Metal-Organic Framework Materials. *J. Am. Chem. Soc.* **2011**, *133*, 5652−5655.
(6) Cavka, J. H.; Jakobsen, S.; Olsbye, U.; Guillou, N.; Lamberti, C.; Bordiga, S.; Lillerud, K. P. A New Zirconium Inorganic Building Brick Forming Metal Organic Frameworks with Exceptional Stability. *J. Am. Chem. Soc.* **2008**, *130*, 13850−13851.
(7) Chen, Z.; Hanna, S. L.; Redfern, L. R.; Alezi, D.; Islamoglu, T.; Farha, O. K. Reticular Chemistry in the Rational Synthesis of Functional Zirconium Cluster-Based MOFs. *Coord. Chem. Rev.* **2019**, *386*, 32−49.
(8) Bai, Y.; Dou, Y.; Xie, L. H.; Rutledge, W.; Li, J. R.; Zhou, H. C. Zr-Based Metal-Organic Frameworks: Design, Synthesis, Structure, and Applications. *Chem. Soc. Rev.* **2016**, *45*, 2327−2367.
(9) Jajko, G.; Kozyra, P.; Gutiérrez-Sevillano, J. J.; Makowski, W.; Calero, S. Carbon Dioxide Capture Enhanced by Pre-Adsorption of Water and Methanol in UiO-66. *Chemistry* **2021**, *27*, 14653−14659.
(10) Jeremias, F.; Lozan, V.; Henninger, S. K.; Janiak, C. Programming MOFs for Water Sorption: Amino-Functionalized MIL-125 and UiO-66 for Heat Transformation and Heat Storage Applications. *Dalton Trans.* **2013**, *42*, 15967−15973.
(11) Schoenecker, P. M.; Carson, C. G.; Jasuja, H.; Flemming, C. J. J.; Walton, K. S. Effect of Water Adsorption on Retention of Structure and Surface Area of Metal-Organic Frameworks. *Ind. Eng. Chem. Res.* **2012**, *51*, 6513−6519.
(12) Cmarik, G. E.; Kim, M.; Cohen, S. M.; Walton, K. S. Tuning the Adsorption Properties of UiO-66 via Ligand Functionalization. *Langmuir* **2012**, *28*, 15606−15613.
(13) Ko, N.; Hong, J.; Sung, S.; Cordova, K. E.; Park, H. J.; Yang, J. K.; Kim, J. A Significant Enhancement of Water Vapour Uptake at Low Pressure by Amine-Functionalization of UiO-67. *Dalton Trans.* **2015**, *44*, 2047−2051.
(14) Zhang, X.; Shen, B.; Zhu, S.; Xu, H.; Tian, L. UiO-66 and Its Br-Modified Derivates for Elemental Mercury Removal. *J. Hazard. Mater.* **2016**, *320*, 556−563.
(15) Zeng, S.; Lyu, F.; Sun, L.; Zhan, Y.; Ma, F. X.; Lu, J.; Li, Y. Y. UiO-66-NO2 as an Oxygen "Pump" for Enhancing Oxygen Reduction Reaction Performance. *Chem. Mater.* **2019**, *31*, 1646−1654.
(16) Katz, M. J.; Brown, Z. J.; Colón, Y. J.; Siu, P. W.; Scheidt, K. A.; Snurr, R. Q.; Hupp, J. T.; Farha, O. K. A Facile Synthesis of UiO-66, UiO-67 and Their Derivatives. *Chem. Commun.* **2013**, *49*, 9449−9451.
(17) Kim, H.; Yang, S.; Rao, S. R.; Narayanan, S.; Kapustin, E. A.; Furukawa, H.; Umans, A. S.; Yaghi, O. M.; Wang, E. N. Water Harvesting from Air with Metal-Organic Frameworks Powered by Natural Sunlight. *Science* **2017**, *356*, 430−434.
(18) Trapani, F.; Polyzoidis, A.; Loebbecke, S.; Piscopo, C. G. On the General Water Harvesting Capability of Metal-Organic Frameworks under Well-Defined Climatic Conditions. *Microporous Mesoporous Mater.* **2016**, *230*, 20−24.
(19) Kim, S. I.; Yoon, T. U.; Kim, M. B.; Lee, S. J.; Hwang, Y. K.; Chang, J. S.; Kim, H. J.; Lee, H. N.; Lee, U. H.; Bae, Y. S. Metal-Organic Frameworks with High Working Capacities and Cyclic Hydrothermal Stabilities for Fresh Water Production. *Chem. Eng. J.* **2016**, *286*, 467−475.
(20) Jeremias, F.; Fröhlich, D.; Janiak, C.; Henninger, S. K. Water and Methanol Adsorption on MOFs for Cycling Heat Transformation Processes. *New J. Chem.* **2014**, *38*, 1846−1852.
(21) Henninger, S. K.; Jeremias, F.; Kummer, H.; Janiak, C. MOFs for Use in Adsorption Heat Pump Processes. *Eur. J. Inorg. Chem.* **2012**, *2012*, 2625−2634.
(22) De Lange, M. F.; Verouden, K. J. F. M.; Vlugt, T. J. H.; Gascon, J.; Kapteijn, F. Adsorption-Driven Heat Pumps: The Potential of Metal-Organic Frameworks. *Chem. Rev.* **2015**, *115*, 12205−12250.
(23) Canivet, J.; Fateeva, A.; Guo, Y.; Coasne, B.; Farrusseng, D. Water Adsorption in MOFs: Fundamentals and Applications. *Chem. Soc. Rev.* **2014**, *43*, 5594−5617.
(24) Rieth, A. J.; Yang, S.; Wang, E. N.; Dincă, M. Record Atmospheric Fresh Water Capture and Heat Transfer with a Material Operating at the Water Uptake Reversibility Limit. *ACS Cent. Sci.* **2017**, *3*, 668−672.
(25) Kalmutzki, M. J.; Diercks, C. S.; Yaghi, O. M. Metal−Organic Frameworks for Water Harvesting from Air. *Adv. Mater.* **2018**, *6*, 1348−1354.
(26) Furukawa, H.; Gándara, F.; Zhang, Y. B.; Jiang, J.; Queen, W. L.; Hudson, M. R.; Yaghi, O. M. Water Adsorption in Porous Metal-Organic Frameworks and Related Materials. *J. Am. Chem. Soc.* **2014**, *136*, 4369−4381.
(27) Thommes, M.; Morell, J.; Cychosz, K. A.; Fröba, M. Combining Nitrogen, Argon, and Water Adsorption for Advanced Characterization of Ordered Mesoporous Carbons (CMKs) and Periodic Mesoporous Organosilicas (PMOs). *Langmuir* **2013**, *29*, 14893−14902.
(28) Hunter, K. M.; Wagner, J. C.; Kalaj, M.; Cohen, S. M.; Xiong, W.; Paesani, F. Simulation Meets Experiment: Unraveling the Properties of Water in Metal−Organic Frameworks through Vibrational Spectroscopy. *J. Phys. Chem. C* **2021**, *125*, 12451−12460.
(29) Jajko, G.; Gutiérrez-Sevillano, J. J.; Sławek, A.; Szufla, M.; Kozyra, P.; Matoga, D.; Makowski, W.; Calero, S. Water Adsorption in Ideal and Defective UiO-66 Structures. *Microporous Mesoporous Mater.* **2021**, *330*, No. 111555.
(30) Makowski, W.; Ogorzałek, Ł. Determination of the Adsorption Heat of N-Hexane and n-Heptane on Zeolites Beta, L, 5A, 13X, Y and ZSM-5 by Means of Quasi-Equilibrated Temperature-Programmed Desorption and Adsorption (QE-TPDA). *Thermochim. Acta* **2007**, *465*, 30−39.
(31) Makowski, W. Quasi-Equilibrated Temperature Programmed Desorption and Adsorption: A New Method for Determination of the Isosteric Adsorption Heat. *Thermochim. Acta* **2007**, *454*, 26−32.
(32) Sławek, A.; Vicent-Luna, J. M.; Marszałek, B.; Makowski, W.; Calero, S. Ordering of N-Alkanes Adsorbed in the Micropores of AlPO4-5: A Combined Molecular Simulations and Quasi-Equilibrated Thermodesorption Study. *J. Phys. Chem. C* **2017**, *121*, 25292−25302.
(33) Garibay, S. J.; Cohen, S. M. Isoreticular Synthesis and Modification of Frameworks with the UiO-66 Topology. *Chem. Commun.* **2010**, *46*, 7700−7702.
(34) Delley, B. From Molecules to Solids with the DMol3 Approach. *J. Chem. Phys.* **2000**, *113*, 7756.
(35) Perdew, J. P.; Burke, K.; Ernzerhof, M. Generalized Gradient Approximation Made Simple. *Phys. Rev. Lett.* **1996**, *77*, 3865−3868.
(36) Hammer, B.; Hansen, L. B.; Nørskov, J. K. Improved Adsorption Energetics within Density-Functional Theory Using Revised Perdew-Burke-Ernzerhof Functionals. *Phys. Rev. B-Condens. Matter Mater. Phys.* **1999**, *59*, 7413−7421.
(37) Delley, B. Hardness Conserving Semilocal Pseudopotentials. *Phys. Rev. B-Condens. Matter Mater. Phys.* **2002**, *66*, No. 155125.
(38) Frenkel, D.; Smit, B. *Understanding Molecular Simulation: From Algorithms to Applications* 1996.
(39) Wldom, B. Some Topics in the Theory of Fluids. *J. Chem. Phys.* **1963**, *39*, 2808−2812.
(40) Dubbeldam, D.; Calero, S.; Ellis, D. E.; Snurr, R. Q. RASPA: Molecular Simulation Software for Adsorption and Diffusion in Flexible Nanoporous Materials. *Mol. Simul.* **2016**, *42*, 81−101.
(41) Dubbeldam, D.; Torres-Knoop, A.; Walton, K. S. On the Inner Workings of Monte Carlo Codes. *Mol. Simul.* **2013**, *39*, 1253−1292.
(42) Horn, H. W.; Swope, W. C.; Pitera, J. W.; Madura, J. D.; Dick, T. J.; Hura, G. L.; Head-Gordon, T. Development of an Improved Four-Site Water Model for Biomolecular Simulations: TIP4P-Ew. *J. Chem. Phys.* **2004**, *120*, 9665−9678.

https://doi.org/10.1021/acs.jpcc.2c02315
J. Phys. Chem. C 2022, 126, 9185−9194

(43) Mayo, S. L.; Olafson, B. D.; Goddard, W. A. DREIDING: A Generic Force Field for Molecular Simulations. *J. Phys. Chem.* **1990**, *94*, 8897−8909.
(44) Rappe, A. K.; Casewit, C. J.; Colwell, K. S.; Goddard, W. A.; Skiff, W. M. UFF, a Full Periodic Table Force Field for Molecular Mechanics and Molecular Dynamics Simulations. *J. Am. Chem. Soc.* **1992**, *114*, 10024−10035.
(45) Shearer, G. C.; Chavan, S.; Bordiga, S.; Svelle, S.; Olsbye, U.; Lillerud, K. P. Defect Engineering: Tuning the Porosity and Composition of the Metal-Organic Framework UiO-66 via Modulated Synthesis. *Chem. Mater.* **2016**, *28*, 3749−3761.
(46) Valenzano, L.; Civalleri, B.; Chavan, S.; Bordiga, S.; Nilsen, M. H.; Jakobsen, S.; Lillerud, K. P.; Lamberti, C. Disclosing the Complex Structure of UiO-66 Metal Organic Framework: A Synergic Combination of Experiment and Theory. *Chem. Mater.* **2011**, *23*, 1700−1718.
(47) Ghosh, P.; Colón, Y. J.; Snurr, R. Q. Water Adsorption in UiO-66: The Importance of Defects. *Chem. Commun.* **2014**, *50*, 11329−11331.
(48) Wilmer, C. E.; Kim, K. C.; Snurr, R. Q. An Extended Charge Equilibration Method. *J. Phys. Chem. Lett.* **2012**, *3*, 2506−2511.
(49) Gökpinar, S.; Diment, T.; Janiak, C. Environmentally Benign Dry-Gel Conversions of Zr-Based UiO Metal-Organic Frameworks with High Yield and the Possibility of Solvent Re-Use. *Dalton Trans.* **2017**, *46*, 9895−9900.

https://doi.org/10.1021/acs.jpcc.2c02315
J. Phys. Chem. C 2022, 126, 9185−9194